Fluorescence tomography characterization for sub-surface imaging with protoporphyrin IX

Dax Kepshire,[1,*] Scott C. Davis,[1] Hamid Dehghani[1,2],
Keith D. Paulsen,[1] and Brian W. Pogue[1,*]

[1] *Thayer School of Engineering, Dartmouth College, Hanover NH 03755 USA*

[2] *School of Physics, University of Exeter, Stocker Road, Exeter, EX4 4QL, UK*

[*]Corresponding author: Dax@Dartmouth.edu, Pogue@Dartmouth.edu

Abstract: Optical imaging of fluorescent objects embedded in a tissue simulating medium was characterized using non-contact based approaches to fluorescence remittance imaging (FRI) and sub-surface fluorescence diffuse optical tomography (FDOT). Using Protoporphyrin IX as a fluorescent agent, experiments were performed on tissue phantoms comprised of typical in-vivo tumor to normal tissue contrast ratios, ranging from 3.5:1 up to 10:1. It was found that tomographic imaging was able to recover interior inclusions with high contrast relative to the background; however, simple planar fluorescence imaging provided a superior contrast to noise ratio. Overall, FRI performed optimally when the object was located on or close to the surface and, perhaps most importantly, FDOT was able to recover specific depth information about the location of embedded regions. The results indicate that an optimal system for localizing embedded fluorescent regions should combine fluorescence reflectance imaging for high sensitivity and sub-surface tomography for depth detection, thereby allowing more accurate localization in all three directions within the tissue.

©2008 Optical Society of America

OCIS codes: (170.0170) Medical optics and biotechnology; (170.0110) Imaging systems; (170.3010) Image reconstruction techniques; (170.3880) Medical and biological imaging; (170.6960) Tomography; (100.3190) Inverse problems.

References and links

1. W. P. Stummer, Uwe, T. Meinel, O. D. Wiestler, F. Zanella, and H.-J. Reulen, "Fluorescence-guided surgery with 5-aminolevulinic acid for resection of malignant glioma: a randomised controlled multicentre phase III trial " Lancet Oncol. **7**, 392-401 (2006).
2. A. Bogaards, A. Varma, S. P. Collens, A. Lin, A. Giles, V. Yang, J. M. Bilbao, L. D. Lilge, P. J. Muller, and B. C. Wilson, "Increased Brain Tumor Resection Using Fluorescence Image Guidance in a preclinical Model " Lasers Surg. Med. **35** (2004).
3. D. S. Kepshire, S. C. Davis, H. Dehghani, K. D. Paulsen, and B. W. Pogue, "Sub-Surface Diffuse Optical Tomography can Localize Absorber and Fluorescent Objects but Recovered Image Sensitivity is Non-Linear with Depth," Appl. Opt. **46**, 1669-1678 (2007).
4. J. S. Reynolds, T. L. Troy, R. H. Mayer, A. B. Thompson, D. J. Waters, K. K. Cornell, P. W. Snyder, and E. M. Sevick-Muraca, "Imaging of spontaneous canine mammary tumors using fluorescent contrast agents," Photochem. Photobiol. **70**, 87-94 (1999).
5. V. Ntziachristos, J. Ripoll, L. V. Wang, and R. Weissleder, "Looking and listening to light: the evolution of whole-body photonic imaging," Nat. Biotechnol. **23**, 313-320 (2005).
6. V. Ntziachristos, C. Bremer, and R. Weissleder, "Fluorescence imaging with near-infrared light: new technological advances that enable in vivo molecular imaging," Eur. Radiol. **13**, 195-208 (2003).
7. E. M. Sevick-Muraca, J. P. Houston, and M. Gurfinkel, "Fluorescence-enhanced, near infrared diagnostic imaging with contrast agents," Curr. Op. Chem. Biol. **6**, 642-650 (2002).
8. B. W. Pogue, S. L. Gibbs, and B. Chen, "Fluorescence Imaging In Vivo: Raster Scanned Point-Source Imaging Provides More Accurate Quantification than Broad Beam Geometries," Tech. Cancer Res. Treat. **3**, 15-21 (2004).
9. A. M. De Grand and J. V. Frangioni, "An operational near-infrared fluorescence imaging system prototype for large animal surgery," Tech. Cancer Res. Treat. **2**, 553-562 (2003).
10. E. E. Graves, R. Weissleder, and V. Ntziachristos, "Fluorescence molecular imaging of small animal tumor models," Curr. Molec. Med. **4**, 419-430 (2004).

11. V. Ntziachristos, A. G. Yodh, M. Schnall, and B. Chance, "Concurrent MRI and diffuse optical tomography of breast after indocyanine green enhancement," PNAS USA **97**, 2767-2772 (2000).
12. B. W. Pogue, S. P. Poplack, T. O. McBride, W. A. Wells, O. K. S., U. L. Osterberg, and K. D. Paulsen, "Quantitative Hemoglobin Tomography with Diffuse Near-Infrared Spectroscopy: Pilot Results in the Breast," Radiol. **218**, 261-266 (2001).
13. V. Ntziachristos, A. G. Yodh, M. D. Schnall, and B. Chance, "MRI-guided diffuse optical spectroscopy of malignant and benign breast lesions," Neoplasia **4**, 347-354 (2002).
14. M. Franceschini and D. A. Boas, "Noninvasive measurement of neuronal activity with near-infrared optical imaging," NeuroImage **21**, 372-386 (2004).
15. J. C. Hebden, A. Gibson, R. M. Yusof, N. Everdell, E. M. Hillman, D. T. Delpy, S. R. Arridge, T. Austin, J. H. Meek, and J. S. Wyatt, "Three-dimensional optical tomography of the premature infant brain," Phys. Med. Biol. **47**, 4155-4166 (2002).
16. A. Bluestone, G. Abdoulaev, C. Schmitz, R. Barbour, and A. Hielscher, "Three-dimensional optical tomography of hemodynamics in the human head," Opt. Express **9**, 272-286 (2001).
17. J. P. Culver, T. Durduran, D. Furuya, C. Cheung, J. H. Greenberg, and A. G. Yodh, "Diffuse optical tomography of cerebral blood flow, oxygenation, and metabolism in rat during focal ischemia," J. Cereb. Blood Flow Met. **23**, 911-924 (2003).
18. H. Xu, H. Dehghani, B. W. Pogue, R. F. Springett, K. D. Paulsen, and J. F. Dunn, "Near-infrared imaging in the small animal brain: optimization of fiber positions," J. Biomed. Opt. **8**, 102-110 (2003).
19. V. Ntziachristos, C. H. Tung, C. Bremer, and R. Weissleder, "Fluorescence molecular tomography resolves protease activity in vivo," Nat. Med. **8**, 757-760 (2002).
20. S. A. Friesen, G. O. Hjortland, S. J. Madsen, H. Hirschberg, O. Engebraten, J. M. Nesland, and Q. Peng, "5-Aminolevulinic acid-based photodynamic detection and therapy of brain tumors," Int. J. Oncol. **21**, 577-582 (2002).
21. B. W. Pogue, T. McBride, U. Osterberg, and K. Paulsen, "Comparison of imaging geometries for diffuse optical tomography of tissue," Opt. Exp. **4**, 270-286 (1999).
22. J. Ripoll, R. B. Schulz, and V. Ntziachristos, "Free-space propagation of diffuse light: theory and experiments," Phys. Rev. Lett. **91**, 5 (2003).
23. S. C. Davis, B. W. Pogue, H. Dehghani, and K. D. Paulsen, "Contrast-detail analysis characterizing diffuse optical fluorescence tomography image reconstruction," J. Biomed. Opt. Letters **10**, 1-3 (2005).
24. K. D. Paulsen and Jiang H., "Spatially varying optical property reconstruction using a finite element diffusion equation approximation," Med. Phys. **22**, 691-701 (1995).
25. M. S. Patterson and B. W. Pogue, "Mathimatical model for time-resolved and frequency-domain fluorescence spectroscopy in biological tissues," Appl. Opt. **33**, 1963-1974 (1994).
26. B. W. Pogue, T. O. McBride, J. Prewitt, U. L. Osterberg, and K. D. Paulsen, "Spatially variant regularization improves diffuse optical tomography," Appl. Opt. **38**, 2950-2961 (1999).
27. C. Sheng, P. J. Hoopes, T. Hasan, and B. W. Pogue, "Photobleaching-based Dosimetry Predicts Deposited Dose in ALA-PpIX PDT of Rodent Esophagus," Photochem. Photobiol. **83**, 738-748 (2007).
28. X. Song, B. W. Pogue, S. Jiang, M. M. Doyley, H. Dehghani, T. D. Tosteson, and K. D. Paulsen, "Automated region detection based on the contrast-to-noise ratio in near-infrared tomography," Appl. Opt. **43**, 1053-1062 (2004).
29. D. Kepshire, S. Gibbs, S. Davis, H. Dehghani, K. D. Paulsen, and B. W. Pogue, "Sub-surface Fluorescence Imaging of Protoporphyrin IX with B-Scan Mode Tomography," Proc. SPIE **6139**, In Press (2006).
30. A. Soubret, J. Ripoll, and V. Ntziachristos, "Accuracy of Fluorescent Tomography in thePresence of Heterogeneities: Study of theNormalized Born Ratio," IEEE Trans. Med. Imag. **24**, 1377-1386 (2005).
31. S. C. Partridge, J. E. Gibbs, Y. Lu, L. J. Esserman, D. Tripathy, D. S. Wolverton, H. S. Rugo, E. S. Hwang, C. A. Ewing, and N. M. Hylton, "MRI measurements of breast tumor volume predict response to neoadjuvant chemotherapy and recurrence-free survival," Am. J.Roentgenol. **184**, 1774-1781 (2005).
32. R. L. Barbour, H. L. Graber, J. Chang, S. S. Barbour, P. C. Koo, and R. Aronson, "MRI-Guided Optical Tomography: Prospects and Computation for a New Imaging Method," IEEE Comp. Sci. Eng. **2**, 63-77 (1995).
33. B. Brooksby, B. W. Pogue, S. Jiang, H. Dehghani, S. Srinivasan, C. Kogel, T. D. Tosteson, J. Weaver, S. P. Poplack, and K. D. Paulsen, "Imaging Breast Adipose and Fibroglandular Tissue Molecular Signatures using Hybrid MRI-Guided Near-Infrared Spectral Tomography," PNAS USA **103**, 8828-8833 (2006).
34. B. Brooksby, S. Jiang, H. Dehghani, B. W. Pogue, K. D. Paulsen, J. Weaver, C. Kogel, and S. P. Poplack, "Combining near infrared tomography and magnetic resonance imaging to study in vivo breast tissue: implementation of a Laplacian-type regularization to incorporate magentic reasonance structure," J. Biomed. Opt. **10**, 0515041-0515010 (2005).
35. Q. Zhu, N. Chen, and S. H. Kurtzman, "Imaging tumor angiogenesis by use of combined near-infrared diffusive light and ultrasound," Opt. Lett. **28**, 337-339 (2003).
36. Q. Zhu, S. H. Kurtzma, P. Hegde, S. Tannenbaum, M. Kane, M. Huang, N. G. Chen, B. Jagjivan, and K. Zarfos, "Utilizing optical tomography with ultrasound localization to image heterogeneous hemoglobin distribution in large breast cancers," Neoplasia **7**, 263-270 (2005).
37. D. Piao, H. Xie, W. Zhang, J. Krasinski, G. Zhang, H. Dehghani, and B. W. Pogue, "Endoscopic, rapid near-infrared optical tomography," Opt. Lett. **31**, 2876-2878 (2006).
38. T. J. Farrell, M. S. Patterson, and B. C. Wilson, "A diffusion theory model of spatially resolved, steady-state diffuse reflectance for the noninvasive determination of tissue optical properties," Med. Phys. **19**, 879-888 (1992).

39. B. W. Pogue, M. S. Patterson, H. Jiang, and K. D. Paulsen, "Initial assessment of a simple system for frequency domain diffuse optical tomography," Phys. Med. Biol. **40**, 1709-1729 (1995).
40. B. W. Pogue, S. Geimer, T. O. McBride, S. Jiang, U. L. Österberg, and K. D. Paulsen, "Three-dimensional Simulation of Near-Infrared Diffusion in Tissue: Boundary Condition and Geometry Analysis For Finite Element Image Reconstruction," Appl. Opt. **40**, 588-600 (2001).
41. H. Dehghani, B. W. Pogue, J. Shudong, B. Brooksby, and K. D. Paulsen, "Three-dimensional optical tomography: resolution in small-object imaging," Appl. Opt. **42**, 3117-3128 (2003).
42. H. Dehghani, B. W. Pogue, S. P. Poplack, and K. D. Paulsen, "Multiwavelength three-dimensional near-infrared tomography of the breast: initial simulation, phantom, and clinical results," Appl. Opt. **42**, 135-14(2003).

1. Introduction

Fluorescence-guided surgical resection of malignant glioma has recently been shown to significantly improve progression-free survival when compared to conventional white-light surgical procedures [1, 2]. The imaging approach adopted in these surgical guidance applications uses the fluorescence provided by preoperative intravenous injection of a prodrug, 5-aminolevulinic acid, from which the body biochemically synthesizes Protoporphyrin IX (Pp-IX). The standard technology deployed for guidance in these clinical imaging studies maps the remitted red fluorescence signal at the surface when illuminated with blue light, but does not otherwise exploit sub-surface light propagation which could be used for tomography. In a previous study, it was established that red light excitation and emission could be used for sub-surface tomography, but was not able to quantify the contrast of small objects embedded below the surface of tissue. Only detection was possible, yet no comparison to planar imaging was done [3]. In the present study, the ability to detect sub-surface regions of localized fluorescence was compared using fluorescence diffuse optical tomography (FDOT) and simpler planar surface imaging approaches. The strengths and weaknesses of both surface and subsurface imaging are evaluated empirically as well as quantitatively by performing contrast-to-noise (CNR) and contrast detail analysis on experimental data sets. The potential for a surgical guidance system that incorporates both surface imaging and FDOT is highlighted.

The propagation of visible and NIR light in biological tissue is dominated by absorption and scattering events which inherently impose geometrical and attenuation limitations that make clinical imaging at depth extremely challenging. Fluorescence imaging in a reflectance or remittance geometry, also known as fluorescence remission imaging (FRI), or planar imaging, is a common technique which is often used to create a topological map of the fluorescence intensity at the surface of the specimen. In recent years, this technology has been investigated for detecting lesions in animal models [4-7], [8], and as a surgical guidance probe for large animals [9] and humans [1, 2]. Previously, Graves et al. [10] and Ntziachristos et al. [5] demonstrated the inability to image deep targets embedded in a highly scattering media using planar reflectance and transmission imaging techniques, respectively. In both studies, the planar techniques were contrasted with FDOT in a transmission geometry. The results indicated that imaging with transmission tomography provides superior localization and quantification of the underlying fluorochrome distributions. Unfortunately, this is not always a viable option because tissue has high absorbance and scattering properties in the visible/NIR frequency band, thereby making it difficult to maintain adequate SNR in dense or large tissues. As a result, transmission tomography is primarily limited to small soft tissue volumes, such as the breast.

In terms of clinical practice, sub-surface optical tomography may be the most promising because it allows the excitation and remission light to be delivered and collected from the same tissue surface. To date, sub-surface tomography has been used to non-invasively probe tissue volumes for breast cancer [11-13], brain function [14-16], and small animals models[17-19]. Recently, Kepshire et al. [3] reported a non-linear relationship between recovered target fluorochrome and chromophore concentrations and depth in this geometry. The study also demonstrated that sub-surface tomography can localize embedded fluorescent lesions at depths up to 1 cm with a mean positional accuracy of approximately 1 mm. These

results indicate potential for applications such as surgical guidance, where detection, rather than quantification of embedded lesions is more important. It should be noted that the experiments in [3] were idealized because they considered only infinite object contrast, and thus represent best case conditions for imaging sub-surface inclusions in this geometry.

In this work, the FRI and sub-surface FDOT techniques under investigation were optimized for imaging Protoporphyrin IX (Pp-IX) fluorescence. Pp-IX is preferentially produced in tumor cells through an increase in heme synthesis; its production in the brain has previously been shown to be significantly more abundant in glioma tumors than in the surrounding normal brain parenchyma, with contrasts of tumor to normal tissue near 6:1 being reported [20]. The lesion sizes to be detected are usually in the margins of normal tissue, following otherwise thorough tumor bulk resection. Thus the lesion sizes are not known exactly, but likely to be quite small, and of indeterminate position relative to the resection cavity surface. In this study, which evaluates the performance of FRI and FDOT for surgical guidance applications, experiments were performed using contrasts as low as 3.5:1, and sizes ranging from 2.5 mm up to 10 mm. Results were quantified and compared to assess the detectable contrast and the contrast to noise ratio of each modality.

2. Materials and methods

2.1 Instrumentation

2.1.1 Tomographic imaging

The non-contact fluorescence diffuse optical tomography (FDOT) imaging system illustrated in Fig. 1 (a) was used to collect fluorescence intensity signals in the 'sub-surface reflectance' geometry [21]; that is, with the excitation and emission signals delivered and collected from the same side of the phantom surface. The instrumentation and data calibration components of this system have previously been described in detail by Kepshire et al. [3]. In the present work, a target containing an increased concentration of the Pp-IX fluorophore was submerged in a tissue-simulating liquid phantom, as shown in Fig. 2 (a), and positioned within the imaging plane. Non-contact excitation signals were delivered to the phantom surface using a 635nm collimated diode laser (Model CPS196, Thor Labs) and a pair of orthogonal galvanometers (Model 6220, Cambridge Technology). By dynamically adjusting the position of a single galvanometer, the laser source was made to raster scan along a single plane in the area under examination. Excitation and emission diffuse intensity signals were then separated by a 650nm long pass optical filter (Omega Optical) with a measured rejection ratio of 4 OD, directed through a lens of f 1.2, and collected using a temperature stabilized CCD camera (Sensicam QE, Cooke Corporation). For each source position, 15 'virtual detectors' [22] were created by averaging groups of pixels in the camera's 4cm (y-dimension) x 2.5mm (x-dimension) field-of-view (FOV) on the phantom surface, as shown in Fig. 1 (b). In building each dataset, 16 source positions were used to collect 240 measurements of the fluorescence diffusion along a single 1-D line in the x-y plane. This is illustrated in Fig. 1 (b). The data collected from the location of the active source was omitted to ensure the validity of the diffusion regime. The collected data is then used to reconstruct 2-D images of the subsurface distribution of fluorescence yield in the y-z plane, as shown schematically in Fig. 2 (b).

2.1.2 Surface imaging

Surface imaging systems are most commonly used because they can be created simply using camera achromat lenses and a CCD, and work efficiently and simply. It is possible to create a surface image with the previous raster scanning system, simply by summing up all data from the point scanner, however in practice, the difference in collection optics is also significant. An achromatic lens on a broad beam system source provides different source delivery than a collimated point laser in a scanning system and could affect the results. Thus, to make the comparison true to the differences between these two types of systems, a separate broad beam imaging system was used for the planar imaging. A schematic of the fluorescence broad beam instrumentation is shown in Fig. 1 (b), where for the purposes of this study, the imaging

plane was located above the camera, which is pointing vertically upward. In the reflectance geometry, the surface imaging experiments were performed using the same instrumentation described in the previous 'Tomographic Imaging' section, with the exception of the laser source. Here, a 635nm diode laser with adjustable 2 Watt output power (Power Technology Inc.) was coupled to the fiber optic cable, and was expanded to yield a broad beam light source of approximately 80cm^2. The excitation light was delivered to the bottom surface of the phantom illustrated in Fig. 2 (a) and the resulting diffuse fluorescence was then separated from the excitation light using a 650nm long-pass optical filter. The image was captured by the CCD using a 50ms exposure. The total FOV under consideration for the surface imaging experiments was 1cm (x-dimension) by 4cm (y-dimension); as demonstrated schematically in Fig. 2 (c). The fluence of the laser source was set to 0.8 mW/mm^2, to match the fluence used in the raster scanned tomography approach. This is a high light dose, and leads to photobleaching of the PPIX in vivo which is near 20% of the peak value for 1 minute of irradiation, however since the scanning placement per source location was within this timescale, the error due to photobleaching was limited to less than 20%. PPIX is well known to photobleach rapidly in vivo, more than in phantoms, so that this is an issue which is unavoidable when using this compound.

2.2 Theory of tomographic image formation

FluoroFAST, a custom finite-element based software package [23], utilizes a nonlinear Newton-minimization approach [24] to obtain inverse solutions to the continuous wave diffusion Eqs [25]:

$$\nabla \cdot D_x(\vec{r})\nabla\Phi_x(\vec{r}) - \mu_{ax}(\vec{r})\Phi_x(\vec{r}) = -Q_0(\vec{r}) \tag{1}$$

$$\nabla \cdot D_m(\vec{r})\nabla\cdot\Phi_m(\vec{r}) - \mu_{am}(\vec{r})\Phi_m(\vec{r},\omega) = -\Phi_x(\vec{r})\eta\mu_{af}(\vec{r}) \tag{2}$$

Here, the excitation (*x*) and fluorescence emission (*m*) fields are governed by Eq. (1) and (2) which *c* represents the speed of light in the medium in each case. The diffusion coefficients are given by $D_{x,m} = 1/[3(\mu_{ax,m} + \mu'_{sx,m})]$ where μ_{ax} and μ_{am} are the absorption coefficients and the reduced scattering coefficient, μ_s'. At the excitation wavelength, the isotropic source term at position $\vec{r}$ is given by $Q_0(\vec{r})$. The excitation and emission fields at position $\vec{r}$ are then $\Phi_{x,m}(\vec{r})$. In (2), μ_{af} is the fluorophore absorption , and η represents the fluorescence quantum yield. The inversion method utilizes a spatially variant modified-Tikhonov regularization parameter [26] to minimize the data-model misfit and iteratively recover the optical properties at each node in the finite-element model. Specifically, the optical property update Eq is given by:

$$\partial\mu = \left(\mathfrak{I}^T\mathfrak{I} + \lambda(z)I\right)^{-1}\mathfrak{I}^T\left(\phi_{meas} - \phi_{calc}\right) \tag{3}$$

Here, μ is a generic symbol for the optical property of interest, $\lambda(z)$ is a spatially variant regularization parameter; ϕ_{meas}^i is the measured intensity data, ϕ_{calc}^i is the computed model intensity data, *I* is the identity matrix, and $\mathfrak{I}$ is the Jacobian matrix. For all of the work presented in this study, a 2% change in the data model mismatch between iterations was used as the stopping criteria. A detailed description of the methodology and numerical procedures has been reported previously [3].
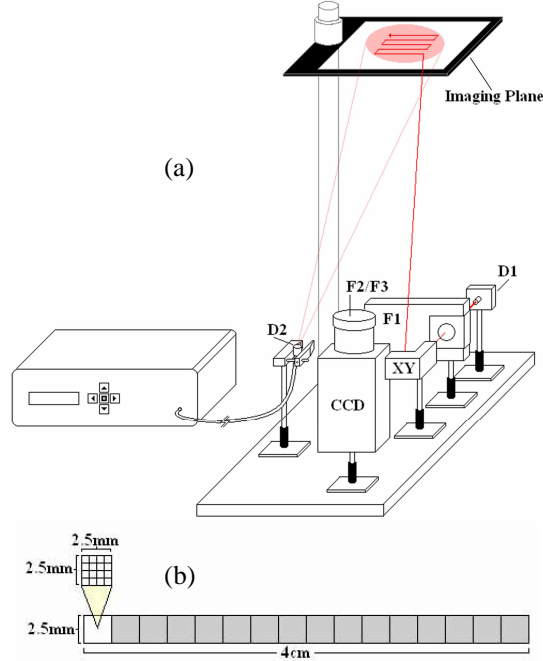
Fig. 1. The experimental FDOT setup is comprised of an excitation light source (D1), two orthogonal galvanometers (XY) for scanning the source position, a filter for attenuating the excitation light (F1), filters for separating the excitation and emission light (F2/F3), and a charge coupled device (CCD) camera for detection. This hardware set up, with the detector camera pointing upwards at a glass plate upon which phantoms and animals can be placed, is shown schematically in (a). The surface imaging experiments utilized a similar hardware configuration, but with a high-power broadbeam laser (D2). A schematic of the virtual detector scheme (b) used for tomography illustrates the intensity from a group of pixels (256) being averaged together to form a virtual detector.

2.3 Tissue simulating phantom experiments

The primary objective of the phantom experiments was to evaluate the ability to image biologically relevant contrasts over a range of depths using both FDOT and FRI. A liquid phantom shown in Fig. 2(a) was filled with water, 2% India ink (a simple black absorbing agent), 5% Tween-20 (a laboratory grade detergent) to create absorption coefficient, $\mu_a = 0.0071$ mm^{-1}, and with 1% Intralipid™ to create reduced scattering coefficient, $\mu_s^{/} = 1.0$ mm^{-1}, to simulate the optical properties of tissue. Using Protoporphyrin IX (Pp-IX) as a fluorophore, the background Pp-IX concentration was fixed at 1 μg/mL, to create additional absorption coefficient due to the fluorophore of $\mu_{af} = 0.002$ mm^{-1}. This concentration was chosen to reflect known values of Pp-IX in vivo [27]. The concentration in the target was systematically increased to yield target to background contrasts of 3.5:1, 5:1, and 10:1. For each contrast, an 8mm diameter cylindrical target was submerged in the phantom and imaged at 5 different depths in the range 0-10 mm. The tomographic data was calibrated [3] and used to recover the subsurface spatial distribution of the fluorescent yield, $\eta\mu_{af}$, which is the product of the fluorophore quantum yield and the fluorescent agent absorption coefficient. The optical properties at the excitation wavelength were assumed to be known. To generate surface images, filtered fluorescence data sets of the ROI under investigation were acquired before, $\phi_{(\hom o\_m)}^{i,j}$, and after, $\phi_{(hetero\_m)}^{i,j}$, Pp-IX was added to the intralipid solution. Surface images $\phi_{fl}^{i,j}$ were then generated by:

$$\phi_{fl}^{i,j} = \left(\phi_{(hetero\_m)}^{i,j} - \phi_{(\hom o\_m)}^{i,j}\right) \tag{3}$$

where i and j correspond to image pixels. By subtracting the background ($\phi_{(\hom o\_m)}^{i,j}$) from the raw fluorescence dataset ($\phi_{(hetero\_m)}^{i,j}$), compensation for the background fluorescence and the excitation light not rejected by the filter was included.
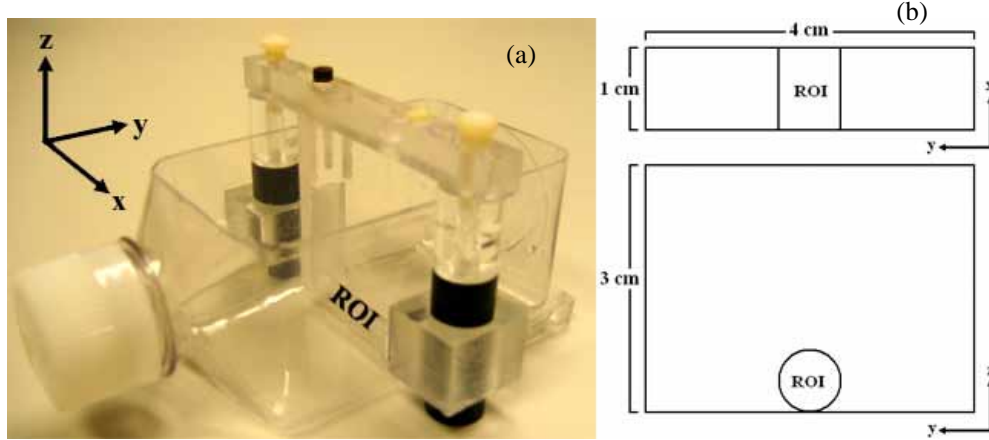

Fig. 2. A photograph of the liquid phantom used in these experiments is shown in (a). All experiments were performed by submerging a cylindrical target in the liquid phantom shown here. Targets of varying diameter were filled with fluorescent contrast agents, positioned at varying depths and imaged using surface imaging and FDOT. In both cases imaging was performed from below; the experimental image dimensions are shown in schematic (b) for FRI (top) and FDOT (bottom).

2.4 Image analysis

Image contrast-to-noise analysis has been used to quantify performance in diffuse optical tomography [23, 28] and fluorescence diffuse optical tomography [23]. Though it avoids the subjective component introduced by a human observer, it remains an appropriate and effective method for quantitatively determine relatively accurate bounds of detectability for a given imaging system. Here, image contrast-to-noise ratio (CNR) was examined as a function of target depth from the surface for both fluorescence tomography and fluorescence surface imaging. In performing contrast-to-noise analysis the following Eq was selected to ensure proper weighting of the noise in the target and background regions [28]:

$$CNR = \frac{\mu_{af}^{ROI} - \mu_{af}^{bkg}}{\left(w_{ROI}\sigma_{ROI}^2 - w_{bkg}\sigma_{bkg}^2\right)} \qquad (4)$$

where μ_{af}^{ROI} & μ_{af}^{bkg} are the mean node values in the target and background respectively, w_{ROI} & w_{bkg} are weighting factors to account for the area of each ROI, and σ_{ROI}^2 & σ_{bkg}^2 are the calculated noise values in the target and background. Specifically, the noise weighting for the background and ROI were calculated as $w_{bkg} = \frac{Area_{bkg}}{\left(Area_{ROI} + Area_{bkg}\right)}$ and $w_{ROI} = \frac{Area_{ROI}}{\left(Area_{ROI} + Area_{bkg}\right)}$ respectively. Image contrast, the relative difference between the fluorescence intensity in the target and the background, was then calculated according to:

$$Contrast = \frac{\mu_{af}^{ROI} - \mu_{af}^{bkg}}{\mu_{af}^{bkg}} \qquad (5)$$

To calculate the contrast and CNR in tomographic images, the image was interpolated onto a 10,000 node mesh. The mean signal and noise in the region of interest (ROI) was computed using the area inside a circle of 4mm radius from the reconstructed centroid location. The entire area outside of each target region was then used to compute the background signal and noise levels. In the surface imaging analysis, the pixel locations corresponding to the target and background were determined from the 'True' white light reflectance image shown in Fig. 6 (top). Examples of the region segmentation used in the ROI analysis are shown in Fig. 3 for tomographic (a) and surface (b) images, respectively.
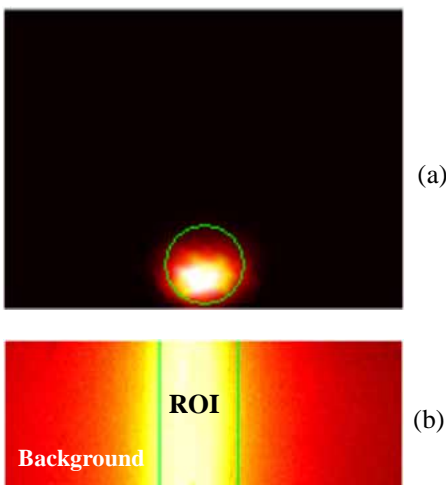

Fig. 3. Examples of the imaged region segmentation used in the CNR and contrast calculations for tomographic (a) and surface (b) images. In the tomographic images, the target ROI was determined based on the position of the recovered centroid whereas the regions were fixed for the broadbeam analysis. The Tomographic image in (a) is a few into the medium, similar to an ultrasound B-scan, but the surface is located at the bottom of the image. The surface image in (b) shows the extended shape of the cylinder as viewed from the bottom surface.

3. Results

3.1 Subsurface fluorescence tomography

Diffuse projections of the fluorescence intensity were collected at the surface of a liquid phantom designed to simulate the optical properties of tissue while the contrast and depth of an 8 mm target were systematically adjusted. Datasets were calibrated and used to reconstruct the sub-surface spatial distribution of fluorescence yield. Image results for a fixed 8 mm target with different depths and contrasts are shown in Fig. 4. A quantitative evaluation of the centroid recovery for this experiment is highlighted in Fig. 5. It is apparent that the target can be localized using sub-surface tomography, but this ability begins to degrade with decreasing contrast. In addition, it is evident that the ability to recover target fluorophore concentration and size is not possible, as indicated by the large variation in these parameters with depth. Overall, the mean centroid error in this set of images was determined to be 0.87 mm within the first 1 cm below the surface when target contrasts of 5:1 and greater were considered.. The centroid results for 3.5:1 contrast were excluded in the quantification of mean error because a large discrepancy was observed between the experimental results presented here and those of a previous simulation study [29]. It is hypothesized that these inconsistencies can be attributed to an inadequate SNR in some of the data because the experiments presented here utilized the same integration scheme for all target contrasts and depths under examination. So, when imaging lower contrasts at depth, only a very small fraction of the camera's dynamic range is being utilized. Exploiting the full dynamic range of the camera is

essential for maintaining a good SNR, but is challenging because the fluorescence intensity rapidly degrades with decreasing target size, contrast, and depth.
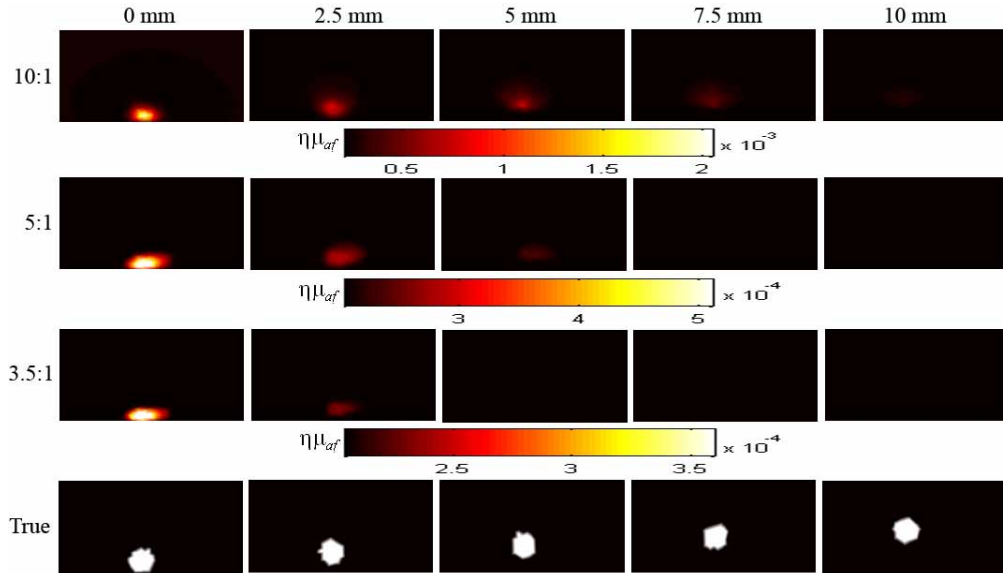

Fig. 4. A representative set of fluorescence image reconstructions in the remission-slab geometry, using a cylindrical region to be imaged. The images are shown as a function of depth into the medium (like an ultrasound image) with the surface at the bottom, and the round circular region being the cylinder shown cut through the middle (bottom). Images were reconstructed from experimental data collected for an 8 mm target submerged in a liquid phantom, when the target had 10:1, 5:1, and 3.5:1 fluorescent contrast with respect to the background. The true target locations are shown at the bottom of the Fig.
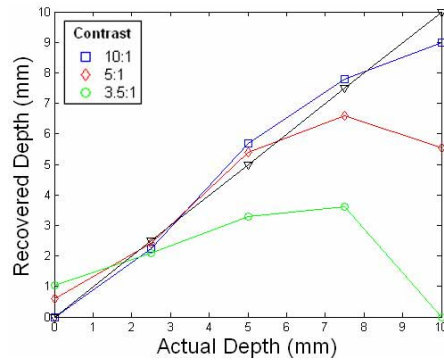

Fig. 5: Experimental fluorescence centroid results when the depth of an 8mm target was varied for contrasts of 10:1, 5:1, and 3.5:1. When contrasts of 5:1 and above were considered, mean positional error in the recovered centroid was determined to be 0.87 mm on average.

3.2 Fluorescence surface imaging

The same tissue simulating liquid phantom experiment was repeated using the surface imaging technique. Results for the case of an 8mm cylindrical target with a range of depths and target-to-background contrasts are shown in Fig. 6. For comparison, a white light image of the empty phantom positioned in the field-of-view under examination, denoted 'True', is shown at the top of this Fig. It is evident that FRI is able to recover the target quite well for all contrasts under examination when it is positioned within 2.5mm of the periphery, but this ability rapidly degrades with distance from the boundary; especially for realistic in-vivo

contrasts below 10:1. When these low contrasts are considered empirically it is apparent that the fluorescence from an embedded target could possibly be misinterpreted as noise or intrinsic fluorophore heterogeneities. Moreover, surface imaging provides no means of quantifying the actual depth of the lesion.
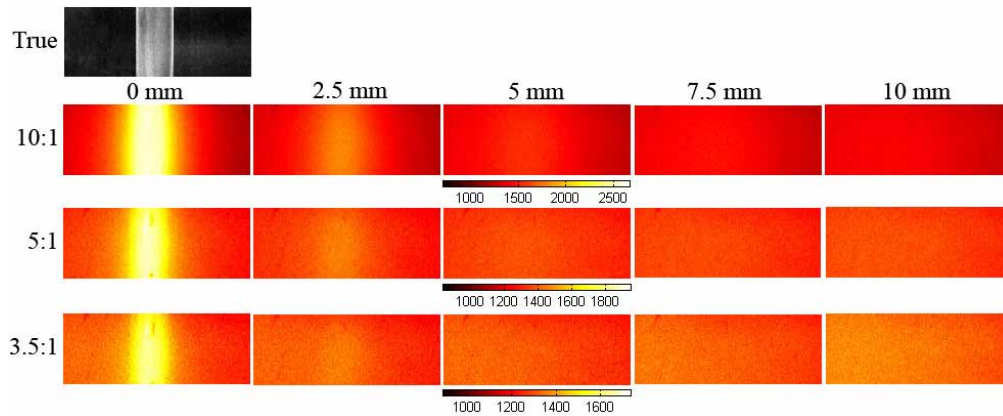

Fig. 6. Experimental fluorescence broad beam imaging results when the depth and target-to-background contrast of an 8mm target was adjusted. It is clear that the ability to recover targets using this technique degrades rapidly with depth below the surface.

There is slight asymmetry in the illumination, due to the finite size of the light source, and the angle of illumination. This is true in almost all broad beam imaging systems, and while it can be seen in the images of Fig.s 3 and 6, especially in the last 10:1 contrast image, it does not significantly affect the conclusions of the experimental work. This asymmetry is more an artifact which must be dealt with in all systems, and can degrade detection of subsurface objects if not properly interpreted as such.

3.3 Image analysis

Image contrast (a) and contrast-to-noise (b) results for the tomographic and surface images are shown in Fig. 7 and Fig. 8, respectively. These Fig.s indicate that the contrast in FDOT is greater than planar imaging, but CNR is substantially better in surface imaging because of the low noise levels. This is not surprising since tomographic images are inherently noisy due to the ill-posed nature of the problem and the non-linear image reconstruction techniques that are involved. The maximum CNR in the tomographic images occurs around a depth of 2.5mm and not at the surface where the SNR is the highest. This may be due to a hypersensitivity near the imaging boundary [29] or photon propagation that does not adhere to the diffusion approximation over short distances. Targets in the 2.5mm depth range yield the best reconstructed images not only in terms of contrast and CNR, but also in terms of centroid accuracy. Planar imaging measurements indicate an increasing trend in CNR around target depths of 7.5 to 10 mm in the surface imaging experiment. This may be attributed to the incident angle of the laser beam orientation relative to the phantom. In both cases, image contrast and CNR are governed by the depth of the target and the tissue/phantom optical properties because of the diffuse nature of the light propagation.

There is a slight increase in CNR values in Fig. 8(b) when the object is at deeper depths, and this was attributed to a decrease in spatial uniformity, or 'noise' rather than an true increase in contrast. This slight increase is an experimental artifact, due to the finite size of the source beam, rather than a true increase in CNR which is reliably reflecting detection of the object embedded below.
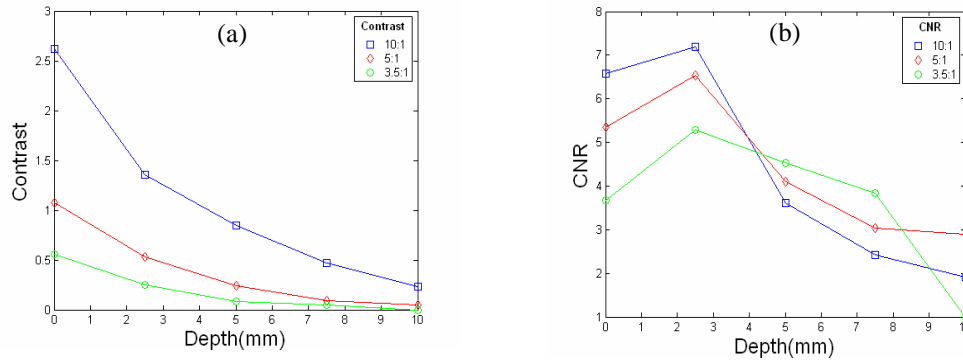
Fig. 7. Experimental fluorescence tomography recovered contrast (a) and recovered CNR (b) results when the depth of an 8mm target was varied for contrasts of 10:1, 5:1, and 3.5:1.
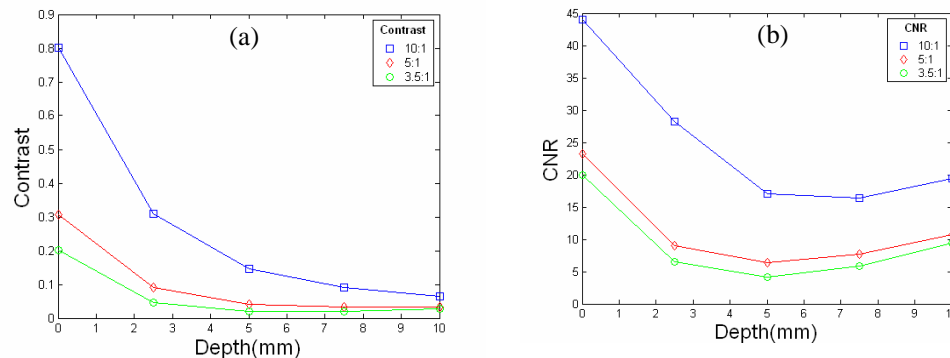

Fig. 8. Experimental recovered contrast (a) and recovered CNR (b) analysis for the set of fluorescence broad beam images depicted in Fig. 6.

4. Discussion

Although the inability to image embedded fluorescence targets at depth using planar imaging techniques has previously been demonstrated for transmission [5] and reflectance [10] geometries, the performance of fluorescence reflectance imaging (FRI) has yet to be quantitatively compared to sub-surface FDOT. Results from this study indicate that surface-based imaging is as beneficial as tomography when the tumor is or very close to the surface. However, as the target moves deeper into the medium the ability to easily detect the presence of an embedded target in the presence of endogenous background signal degrades rapidly (within millimeters) when surface imaging alone is used. This is readily seen in applications of subsurface imaging of tumors which express green fluorescence protein, where thin tissue layers over the tumor can yield detection of the tumor to be impossible. Although optimized surface imaging techniques have been demonstrated [30, 31], results are not expected to improve to the point where this fundamental problem will be solved, because it is mostly limited by the basic physics of the signal recovery problem. Conversely, by compensating for the diffuse nature of light using the acquired boundary data and tomographic reconstruction techniques, the distribution of deep, highly scattered fluorochrome distributions can be more accurately estimated. In both FRI and FDOT, the ability to recover embedded fluorescence lesions within a turbid media is a function of target size, target-to-background contrast, and the optical properties of the medium. Although sub-surface tomography is likely less sensitive to small lesions (less than 4mm), it does have the ability to probe deeper than surface imaging and can provide specific depth information. Additionally, if prior information about the location of the region of interest below the surface could be provided by ultrasound or CT,

it is feasible for the fluorescence to be quantified with reasonable accuracy. Studies of this a-priori approach to diffuse tomography have been ongoing for sometime [32-34], with promising results shown for transmission imaging of breast cancers [35, 36].

Sub-surface tomographic imaging devices closely resemble clinically accepted technologies such as endoscopic and surgical microscope systems, making them more easily incorporated into clinical practice. Recently we have shown that endoscopic methods can be used in subsurface tomography for absorption and scatter based imaging [37]; hence, the concept of using endscopic imaging to perform both surface imaging and sub-surface tomography is a clear next step. This approach to imaging would provide both the 2 dimensional localization from the surface imaging, as well as the depth localization in the 3rd dimension offered by tomography. Intrasurgically, one could envision using the tomography simply to detect residuals and then the surface imaging to isolate the exact margins of the sub-surface lesions. The only additional technological feature required is a raster scanned source position. The need for tools which improve fluorescence surgical-guidance of glioma resection is strong, as there is a clear indication of benefit to the patient, as well as an indication that such surgical guidance may benefit the surgeon in training them to find hidden parts of the tumor [1]. As such systems emerge, the quality, linearity and sensitivity limits of sub-surface tomography must be determined for each specific geometry. Based upon the data reported here, it appears likely that sub-surface tomography with diffuse light will be limited to approximately 1 cm of depth sensing, unless more data can be acquired through an additional structural imaging modality.

It should be noted that broad beam imaging can actually be created by a linear summation of the tomographic data collected during raster scanning of the source for all detection points. If the detection channel is summed for all source positions, then in the center of the imaging field, this becomes identical to the diffuse planar imaging case. This approximation breaks down near the edges of the field, where the source summation effect is then asymmetric, and not truly diffuse from all directions. Nonetheless, a nearly complete planar image and a tomographic image could both be developed using a single raster scanning system. Development of this type of combined approach to imaging both planar and tomographic images could be implemented.

It is possible that the limitations of the experiments and simulations here have led to inaccurate representation of how planar or sub-surface tomography could perform in vivo. For example, the diffusion modeling is a limited representation of the light distribution, however this will mainly affect the representation near the surface and within the first 3-4 mm of tissue, as shown by Farrell et al[38]. Use of Monte Carlo or Radiation Transport models to simulate the forward data would undoubtedly lead to more accurate images, yet these cannot reliably be used in vivo, as the spatial map of the anisotropy coefficient and not the phase function cannot be readily known. So, while diffusion modeling limits the imaging system performance, it is likely the only realistic solution for tomography imaging of tissue.

Similarly the use of 2-Dimensional reconstructions is a limitation which is often cited as being limiting, yet it is well known that 3D reconstruction performs considerably less accurately than 2D does, in diffuse tomography [39-42]. Alternatively there was a limitation that there was glass between the tissue phantom and the imaging lenses and sources in this study, and light piping laterally in the glass could have led to a degradation in image performance, however previous phantom studies indicated that this would not be a major problem in our case. However the presence of the flat imaging field is also the best case scenario for planar imaging, and so having the flat field with a known depth of the objects was important for the study accuracy. Removal of the glass plate would have likely increased the accuracy of recovery of tomographic data most, as the light piping is most problematic when taking measurements at farthest source-detector distances where the signal is weakest. Thus, without the glass, it is likely that the tomography images would be slightly improved and resolve objects to slightly deeper depths. Nevertheless, the overall conclusions of the study would not be altered with these changes. Better resolution of near field objects is best with

planar imaging, and resolution of deeper seated objects will likely always be best with tomographic with quantification not likely being possible for either case.

Finally, perhaps the most important piece of the rationale for this study is that fluorescence imaging with ALA-induced PpIX has shown potential success in surgical therapy, since the fluorescence measurements can be acquired in real-time [1]. In addition, 5-ALA has been shown to be taken up preferentially in the malignant Glioma cells, resulting in typical Protoporphyrin IX induced tumor to normal fluorescence contrasts in excess of 5:1. The addition of depth information to the surface fluorescence imaging of PPIX would potentially improve the surgeon's ability to gage depth and enable the removal of thicker tissues in the process. The low production of PPIX in the normal brain provides a contrast level in malignancy which is known to be between 3:1 to 10:1; therefore, the detection of diseased tissues at the depths and contrasts studied here appears to be realistic. In vivo studies of FDOT in brain tissue is the next step in assessing the capabilities of this technology. Endogenous fluorescence from the brain is quite low, and so surgical systems to image this are generally not limited by background signal but by low signal intensity. Future work should focus on optimizing the imaging of such low light signals in a heterogeneous environment such as brain tissue imaging, and also analyze the spatial constraints which apply in the neurosurgery environment which will affect the capabilities for diffuse fluorescence tomography.

5. Conclusions

Based on the results presented here, an optimal surgical guidance system would utilize both surface imaging and sub-surface tomography, particularly in the case of resection of residual disease, where the ROI is not necessarily located on the surface. Sensitivity to objects at depths down to about 1 cm can be achieved for anticipated contrast levels. Neurosurgical tumor resection under combined FRI/FDOT guidance has the potential to improve the number of full resections, as a FDOT based system should be capable of localizing residual tumors along the depth coordinate. The exact useful depth of which a neurosurgeon would use a fluorescence tomography system to remove tissue beyond which can be seen visually is not fully known, since the clinical study has not been done, however it seems as though additional resection beyond 1 cm would be unlikely. However the key value in FDOT versus existing FRI-guided resection is in finding deeper regions of tumor which may be obscured by overlying blood or tissue and the PPIX fluorescence is simply too weak to be viewed by the surgeon. In these cases the added value of tomography can only be determined if the system is used to determine if cases exist where additional tumors in the margin can be found. It is well known that local recurrence of the tumor is very high, indicating that remaining tumor areas are possibly present. The greatest challenges limiting FDOT from serving as a surgical guide is real-time operation and the expected complexity of the surface geometry. Recognition of the tradeoff in size, depth and contrast is an important issue which must be understood as a limiting factor in the sensitivity of these type of systems. Any decrease in size, contrast or depth will decrease the detected signal exponentially. Though this can be overcome somewhat using FDOT imaging, the response to objects at different depths is still non-linear.

Acknowledgments